J. Fluid Mech. (2024), *vol*. 999, A35, doi:10.1017/jfm.2024.968

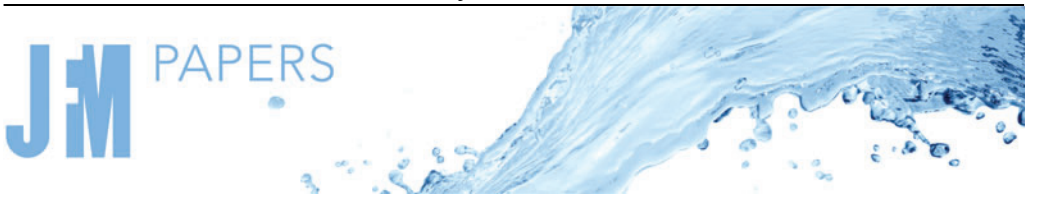

Side-heated Rayleigh–Bénard convection

Jinzi Mac Huang[1,2,†] **and Jun Zhang**[1,2,3,†]

[1]NYU-ECNU Institute of Physics and Institute of Mathematical Sciences, New York University Shanghai, Shanghai 200124, China

[2]Applied Math Lab, Courant Institute, New York University, New York, NY 10012, USA

[3]Department of Physics, New York University, New York, NY 10003, USA

(Received 22 July 2024; revised 28 September 2024; accepted 1 October 2024)

Unlike in solids, heat transfer in fluids can be greatly enhanced due to the presence of convection. Under gravity, an unevenly distributed temperature field results in differences in buoyancy, driving fluid motion that is seen in Rayleigh–Bénard convection (RBC). In RBC, the overall heat flux is found to have a power-law dependence on the imposed temperature difference, with enhanced heat transfer much beyond thermal conduction. In a bounded domain of fluid such as a cube, how RBC responds to thermal perturbations from the vertical sidewall is not clear. Will sidewall heating or cooling modify flow circulation and heat transfer? We address these questions experimentally by adding heat to one side of the RBC. Through careful flow, temperature and heat flux measurements, the effects of adding side heating to RBC are examined and analysed, where a further enhancement of flow circulation and heat transfer is observed. Our results also point to a direct and simple control of the classical RBC system, allowing further manipulation and control of thermal convection through sidewall conditions.

Key words: Bénard convection, buoyancy-driven instability

1. Introduction

Rayleigh–Bénard convection (RBC) has been studied extensively in the past few decades (Tilgner, Belmonte & Libchaber 1993; Belmonte, Tilgner & Libchaber 1994; Niemela *et al.* 2000; Funfschilling *et al.* 2005; Ahlers, Grossmann & Lohse 2009; Lohse & Xia 2010) for its vastly broad applications in geophysics (Zhong & Zhang 2005; Meakin & Jamtveit 2010; Huang *et al.* 2018; Wang & Zhang 2023; Huang 2024), solar physics (Nordlund 1985; Stein & Nordlund 1989; Dudok de Wit *et al.* 2020), atmospheric science

† Email addresses for correspondence: machuang@nyu.edu, jz11@nyu.edu

(Emanuel 1994; Salmon 1998) and ocean dynamics (Jorgensen & LeMone 1989; Vallis 2006). In RBC, a domain of fluid is heated from below and cooled from above, so the near-boundary fluid is either warmed up or cooled off, leading to thermal convection. As the warm and cold fluids move between the top and bottom plates, they effectively create an upward heat flux. At a fixed bottom-to-top temperature difference ΔT, this convective heat transfer rate Q_{conv} is much greater than that which would pass through a quiescent fluid body, Q_{cond}, which is the so-called conductive heat transfer rate. Defined as the ratio between the convective and conductive heat transfer rates, the Nusselt number $Nu = Q_{conv}/Q_{cond}$ measures the heat-passing capability in RBC, which depends on imposed control parameters such as the Rayleigh number $Ra = \alpha g L^3 \Delta T/(\kappa \nu)$ and the Prandtl number $Pr = \nu/\kappa$. Here, $g, L, \alpha, \kappa, \nu$ are the acceleration due to gravity, fluid depth, thermal expansion coefficient, thermal diffusivity and kinematic viscosity, respectively.

Once a fluid and its containing geometry are given, the heat flux is uniquely determined by the imposed temperature difference ΔT. In particular, the famous scaling relationship $Nu \propto Ra^{\beta}$ has been observed in the range from $Ra = 10^6$ to $Ra = 10^{14}$ (Niemela *et al.* 2000; Funfschilling *et al.* 2005), despite local deviations. Grossmann and Lohse (Grossmann & Lohse 2000; Ahlers *et al.* 2009; Stevens *et al.* 2013) developed a theory that incorporates the heat transfer contributed by both the thermal boundary layers and the bulk, revealing a *Nu*–*Ra* relationship that has been found to be consistent with experiments in a large range of parameters.

At a given Rayleigh number, a controllable *Nu* is often desired; anomalies that deviate from the usual scaling laws found in nature also demand explanations (Barry 1992). In the past, there have been many attempts to modify the *Nu*–*Ra* dependency. For example, surface roughness was added to the boundary, which modifies the boundary layer structure and enhances the Nusselt number (Du & Tong 1998; Jiang *et al.* 2018). Adding rotation to the entire fluid changes the bulk flow structure (Stevens *et al.* 2009; Zhong *et al.* 2009; Zhong & Ahlers 2010) and increases the Nusselt number at moderate rotation rate. Stronger confinement on the convective fluid increases the flow structure coherence (Xia & Lui 1997; Chong & Xia 2016; Huang & Xia 2016), and leads to a higher Nusselt number. Bao *et al.* (2015) reported a strong *Nu* enhancement when vertical partition walls are inserted in the bulk fluid. There, the convective fluid self-organizes and circulates around these partitions, intruding into the thermal boundary layers and leading to increased heat flux.

Inspired by the fact that large-scale circulation can be induced by an imposed horizontal temperature gradient (Belmonte, Tilgner & Libchaber 1995), we have demonstrated that the addition of horizontal flux can greatly enhance the large-scale circulation and heat transfer in RBC. In that work (Huang & Zhang 2022), a pair of heating–cooling vertical walls is added so a net horizontal flux can flow through the RBC cell. While such a study is numerically feasible, it is difficult to add and remove the same amount of heat experimentally. We thus focus only on the side-heating effect here, and demonstrate experimentally how an added horizontal flux can change the dynamical and thermal properties of RBC.

In this study, a classical RBC system in a cubical domain is perturbed by a heat flux injected from one of its four vertical sides, as shown in figure 1(*a*). During each experiment, the top cooling temperature T_t is fixed, while *Ra* and *Nu* are measured as functions of the side and bottom heating powers Q_s and Q_b. To the best of our knowledge, this unconventional configuration has not been studied in the past, despite many experiments having explored configurations such as sidewall heating–cooling

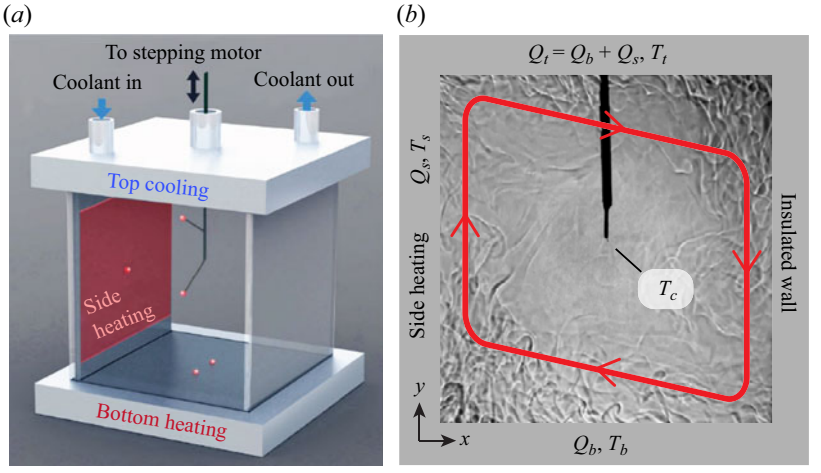

Figure 1. A cubical thermal convection cell with sidewall heating is filled with water as the working fluid. (*a*) Schematic showing the convection cell and the side heater. Thermistors (red dots) are distributed to measure local temperature at various locations. (*b*) Shadowgraph visualizing the density difference and thus the flow structures, with bottom heating power $Q_b = 100$ W, and side-heating power $Q_s = 40$ W. Heat injected from the bottom and the side exits the fluid through the top cooling plate, while the clockwise large-scale circulation is enhanced and dictated by the side heating.

without bottom heating (Belmonte *et al.* 1995), horizontal convection (Miller 1968; Wang & Huang 2005; Hughes & Griffiths 2008), and different sidewall boundary conditions (Stevens, Lohse & Verzicco 2014).

In what follows, we will introduce the experimental set-up in § 2, and show the main results regarding the flow patterns and heat transfer properties of the side-heated RBC in § 3. And finally, in § 4, we will summarize our results and outline future research plans.

2. Experimental set-up

As shown in figure 1(*a*), our experiments are carried out in a cubical cell of side length $L = 20$ cm. The top and bottom plates are made of anodized aluminium that ensures high thermal conductivity and uniform temperature distribution within each plate. In the top plate, coolant water is circulated at a constant temperature 40 °C that is regulated by a water circulator. An electrical film heater is embedded in the bottom plate, providing bottom heating to the fluid. To ensure temperature uniformity, both the top and bottom plates are 2.54 cm thick and made of aluminium. Another film heater covered by an aluminium sheet, 2 mm in thickness and in contact with the fluid, is attached to one side of the vertical walls. The covering aluminium sheet is intended to improve temperature uniformity, whose top and bottom edges are cut away by 5 mm in order to prevent a 'short circuit' of heat flowing from/to the boundary layers. During all experiments excluding the flow visualization, insulating materials cover the RBC cell to minimize heat leak. Local temperature is measured by thermistors distributed in the convection cell. As shown in figure 1(*a*), two thermistors measuring the bottom temperature are embedded 0.5 mm below the bottom surface. One thermistor is located at the centre of the side heater to monitor the side temperature, and two thermistors are mounted on a support that can traverse vertically to measure the temperature profile of the fluid.

We perform all temperature and flow measurements at each (Q_b, Q_s), while varying them independently in the range 0–120 W. While the heat mainly transfers through

the fluid, there are three possible heat leaks that may affect our measurements: (1) the conduction beneath the bottom plate; (2) the vertical conduction of heat through the sidewalls; (3) the horizontal heat leak from the sidewalls to the air.

To minimize the conductive heat leak, the bottom plate is placed on top of layers of insulating foam, beneath which a compensating heater is installed so that the temperature gradient in the foam can be monitored and minimized by a PID algorithm. The sidewalls are made of 5 mm thick acrylic, whose thermal conductivity is approximately $0.2\ \mathrm{W\ m^{-1}\ K^{-1}}$. Considering that the typical temperature difference between top and bottom is about $10\,^{\circ}\mathrm{C}$, the vertical conducting power through the sidewalls is estimated as 0.04 W, much smaller than the convective power carried by the fluid.

The main contribution to heat leakage is in fact the heat transfer between the sidewalls and the surrounding air. Typically, the convection cell operates at a bulk temperature $40\,^{\circ}\mathrm{C}$, and the surrounding air is at the room temperature $25\,^{\circ}\mathrm{C}$. The convection cell, when operating, is covered by many layers of aluminium-coated bubble wrap whose total thickness is of the order of 10 cm, and whose conductivity is approximately $0.02\ \mathrm{W\ m^{-1}\ K^{-1}}$. This allows us to estimate the total side leaking power as 0.5 W, which is much smaller than the minimum bottom heating power (10 W) used in the study. Thus the maximum error that we may have in measuring Nu is 5 %, and this error decays inversely with Q_b.

Whenever a control parameter is changed, the system runs for 4 hours to reach a dynamical equilibrium, and each measurement takes another 4 hours to collect data. With degassed water as the working fluid, the system works at a Rayleigh number in the range 3×10^8 to 5×10^9, and Prandtl number in the range 3.4 to 4.1. At this Ra, the convection is turbulent and the large-scale circulation develops spontaneously.

As shown in figure 1(*b*), a shadowgraph of the convecting fluid reveals local density differences and thus provides a visualization of the convective flows. A convex lens with focal length 20 cm converts light from a point source to near-parallel light, which passes through the convection cell and casts a shadow on a translucent screen. Bulk flow speed U can be inferred by tracing the thermal plumes at a given region, which we choose to be 1 cm from the centre of the heated sidewall. This flow speed U represents the strength of the large-scale circulation. Typically, trajectories of 40 thermal plumes are timed and metered during each experiment, so both the mean flow speed and its standard deviation can be calculated.

3. Results

3.1. *Enhanced large-scale circulation and the modified Nu–Ra relationship*

We expect the addition of side heating to enhance the large-scale circulation, and perhaps also to increase the vertical heat transfer rate. As shown in figure 1(*b*), the fluid near the sidewall is heated and becomes lighter, thus forming an upwelling jet that feeds a clockwise large-scale circulation. Therefore, the thermal energy provided by sidewall heating is partly converted into the fluid kinetic energy that enhances the large-scale circulation.

With a constant bottom heating power $Q_b = 100$ W and side-heating power in the range $Q_s = 10$–100 W, the flow speed can be non-dimensionalized as the Reynolds number $Re = UL/\nu$ shown in figure 2(*a*). In figure 2(*a*), the sidewall power is also non-dimensionalized as the power Grashof number $Gr_q = \alpha g L^2 Q_s/(\lambda \nu^2)$, which is a measure of the relative strength between buoyancy and viscous effects (Schlichting & Gersten 2003). Here, λ is

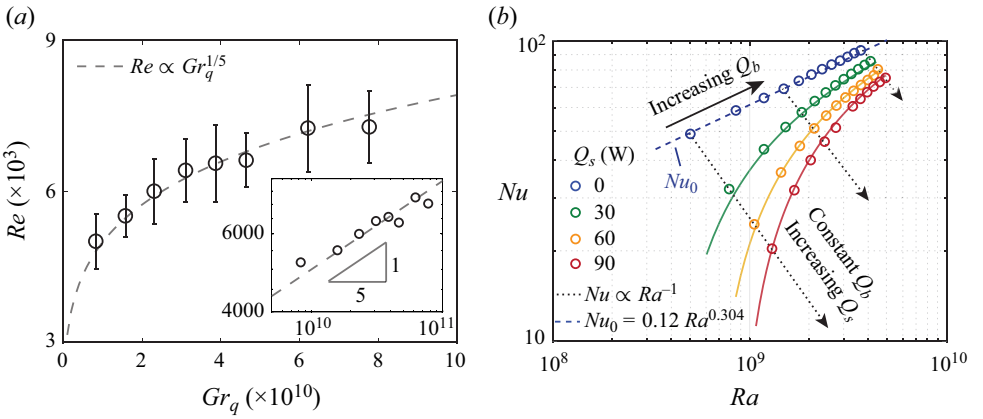

Figure 2. Flow speed and heat transfer measured by Reynolds and Nusselt numbers. (*a*) Plume speed increases with side-heating power. With bottom heating fixed at 100 W, the Reynolds number $Re = UL/\nu$ measured at 1 cm from the sidewall centre shows a monotonic dependence on the power Grashof number Gr_q, consistent with the power-law scaling $Re \propto Gr_q^{1/5}$ from the boundary layer theory (Schlichting & Gersten 2003). The inset shows a logarithmic-scale plot of Reynolds number versus power Grashof number. (*b*) Nusselt number Nu measured at various values of Ra and side-heating power Q_s. The bottom heating power is $Q_b = 10, 20, \ldots, 120$ W. Without side-heating, Nu shows a classical power-law dependence on Ra. Fixing the bottom power, Nu is observed to decrease with increasing side power, while $Nu \propto Ra^{-1}$. Coloured solid curves are the Nu–Ra curve at each fixed Q_s predicted by a theory introduced in § 3.2.

the fluid thermal conductivity. In comparison with the Grashof number $Gr = \alpha g L^3 (T_s - T_\infty)/\nu^2$, the power Grashof number is defined directly through the input heating power Q_s instead of the sidewall temperature difference $T_s - T_\infty$. Far field temperature T_∞ in our case can be taken as the bulk temperature.

The monotonic increase of Re with Gr_q shows that the bulk flow speed is indeed accelerated by the side-heating power. From the boundary layer theory (Schlichting & Gersten 2003), the buoyancy-driven flow speed near a vertical wall scales with the Grashof number Gr as $U \propto Gr^{1/4}$. Using the relationship between the two Grashof numbers (Schlichting & Gersten 2003), namely $Gr \propto Gr_q^{4/5}$, we have the scaling law $Re \propto Gr^{1/4} \propto Gr_q^{1/5}$. This is found to be consistent with our experimental data, as shown in figure 2(*a*). As Q_s reduces to 0, flow velocity drops to the conventional RBC value, which corresponds to $Re \sim 1000$ in our range of Ra (Ahlers *et al.* 2009). Without side heating, the direction of large-scale circulation becomes arbitrary but stays along one of the vertical diagonal planes of the convection cell.

The Nusselt number in the classical cubical RBC is $Nu = Q_b/(\lambda\, \Delta T\, L)$, and figure 2(*b*) shows the Nusselt number measured at various values of Q_s and Q_b. With sidewall heating added, the bulk circulation is enhanced as expected, but the bottom temperature T_b and the resulting $\Delta T = T_b - T_t$ are also found to increase. By definition, $Ra \propto \Delta T$ and $Nu \propto 1/\Delta T$, so an increased ΔT due to side heating causes Ra to increase and Nu to decrease. Moreover, with Q_b fixed at a constant, the product $Nu\, Ra$ is independent of ΔT. Thus the dotted lines in figure 2(*b*) have a common slope -1 in the log-log scale.

As a reference, the Nu–Ra measurement without sidewall heating, $Nu|_{Q_s=0} = Nu_0$ in figure 2(*b*), agrees well with previous experiments (Funfschilling *et al.* 2005; Ahlers *et al.* 2009) and follows a power-law scaling $Nu = 0.12\, Ra^{0.304}$ that is consistent with the Grossmann–Lohse theory. When $Q_s \neq 0$, the observed data deviate from the power-law relation – a simple scaling relationship is absent, particularly at large Q_s.

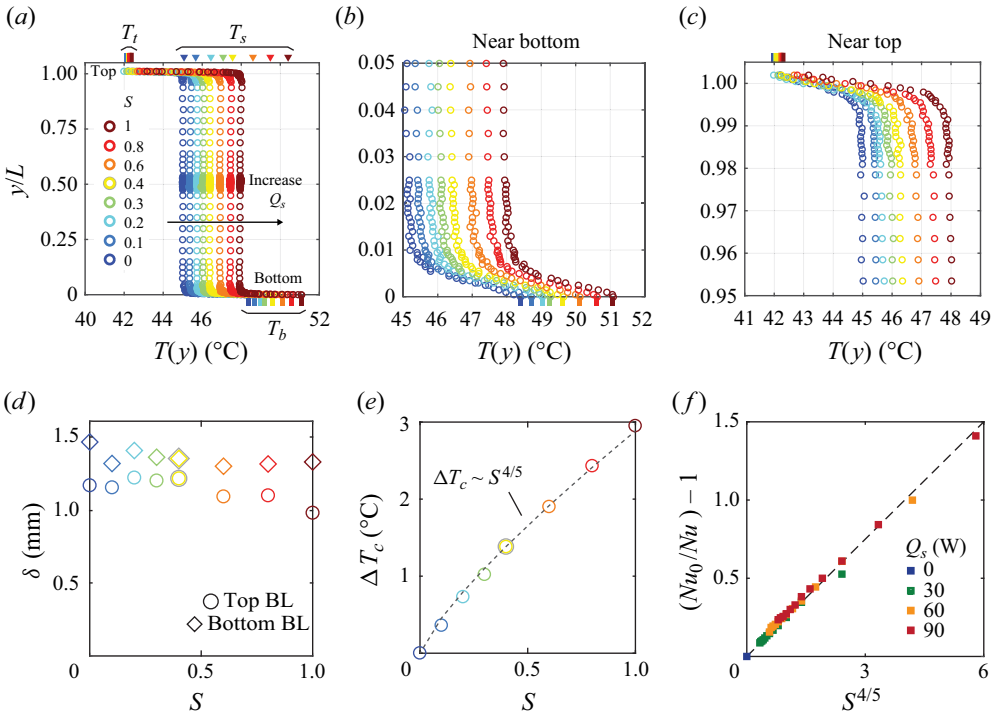

Figure 3. Vertical temperature profiles measured at $Q_b = 100$ W and various values of Q_s, and along the centre vertical line as shown in figure 1(*a*). (*a*) Temperature at different heights. The bulk and bottom temperatures are found to increase with the heating power ratio $S = Q_s/Q_b$. Top, bottom and side temperatures (T_t, T_b and T_s) are marked with ticks and triangles. (*b*) Zoom-in profiles of the bottom thermal boundary layer: T_b increases with the bulk temperature, while the temperature gradient stays nearly constant. (*c*) Zoom-in profiles of the top thermal boundary layer. With top temperature fixed, increased bulk temperature leads to a higher temperature gradient within the boundary layer. (*d*) Thermal boundary layer (BL) thicknesses δ of the top and bottom boundary layers. (*e*) With Q_b fixed, the increase of bulk temperature $\Delta T_c = T_c|_S - T_c|_{S=0}$ has a 4/5 power-law scaling relationship to the side-heating power Q_s. (*f*) Nusselt number as a function of power ratio S, i.e. $Nu_0/Nu = 1 + 0.255^{4/5}$. Plots (*a–e*) share the same colour scheme; (*f*) uses the colour scheme and definition of Nu and Nu_0 as in figure 2(*b*).

3.2. *Temperature measurement explaining the Nu–Ra scaling*

To investigate the modified *Nu–Ra* relationship due to sidewall heating, the vertical temperature distribution is examined along the central vertical axis of the RBC cell shown in figure 1(*a*). Figure 3(*a*) shows several temperature profiles measured at the same bottom power $Q_b = 100$ W but different side power Q_s, where we have defined the heating power ratio as $S = Q_s/Q_b$. On each curve, temperature changes linearly within thermal boundary layers, through which heat transfers by conduction. In the bulk, strong turbulent mixing makes the bulk temperature T_c nearly uniform (Belmonte *et al.* 1994; Ahlers *et al.* 2009), which, together with the bottom temperature T_b, increases with S.

Zooming in near the bottom, figure 3(*b*) shows that the bottom temperature T_b increases with Q_s, while the temperature gradient $\partial T/\partial y$ stays approximately constant within the boundary layer. This is due to the fact that $\partial T/\partial y = -Q_b/(\lambda L^2)$ and the bottom power Q_b is fixed at a constant. The bottom thermal boundary layer thickness $\delta_b = 1.4 \pm 0.1$ mm (or $\delta_b/L = (0.70 \pm 0.05)\%$) is roughly constant for varying S, as shown in figure 3(*d*). This, together with a constant $\partial T/\partial y \sim \Delta T_b/\delta_b$, indicates that the temperature difference

between the bottom and the bulk $\Delta T_b = T_b - T_c$ is not changing with S either, as shown in figure 3(*b*). Figure 3(*c*) shows the zoom-in temperature profiles near the top plate. The addition of side heating Q_s, which has to leave the system through the top plate, leads to a higher temperature gradient $\partial T/\partial y = -(Q_b + Q_s)/(\lambda L^2)$ in the top thermal boundary layer. In our experiment, the top thermal boundary layer thickness is $\delta_t = 1.1 \pm 0.1$ mm (or $\delta_t/L = (0.55 \pm 0.05)\%$), as shown in figure 3(*d*).

Interestingly, the top thermal boundary layer is thinner than the bottom in figure 3(*d*), even when $S = 0$. This is the opposite of the classic RBC, where the non-Boussinesq effect of working fluid makes the bulk warmer and the bottom thermal boundary layer thinner (Zhang, Childress & Libchaber 1997). We have confirmed that this anomaly is a consequence of adding the aluminium side heater, which both conducts heat and modifies the flow structure even when the heating is off. For $S \neq 0$, the boundary layer thickness also varies in space, so the temperature distribution shown in figure 3 only reflects a local profile covered by the range of moving thermistors. To better understand the temperature and flow distributions in the side-heated RBC, we are currently working on a numerical study that may provide further insight.

As the only variable in $Nu = Q_b/(\lambda\,\Delta T\,L)$ is ΔT when holding Q_b constant, understanding how ΔT depends on S can directly explain how Nu depends on S. From the data shown in figure 3(*b*), the bottom to bulk temperature difference stays unchanged while the bulk temperature increases with S. Therefore, the increase of bulk temperature $\Delta T_c(S) = T_c|_S - T_c|_{S=0}$ directly contributes to an increased bottom–top temperature difference ΔT. As shown in figure 3(*e*), the bulk temperature change has a scaling $\Delta T_c \propto S^{4/5}$, which is a direct consequence of the scaling $Gr \propto Gr_q^{4/5}$ discussed earlier, in § 3.1.

We therefore estimate $\Delta T = (1 + \gamma S^{4/5})\,\Delta T|_{S=0}$, where γ is a positive constant. Substituting this into the definition of the Nusselt number, we have $Nu_0/Nu(S) = \Delta T/\Delta T|_{S=0} = 1 + \gamma S^{4/5}$. Plotting $Nu_0/Nu - 1$ against $S^{4/5}$, all the data points in figure 2(*b*) land on a straight line, as shown in figure 3(*f*), whose slope is $\gamma \approx 0.25$. We can also apply this relation to $S = Q_s/Q_b$ with fixed Q_s and varying Q_b, which is shown as the *Ra*–*Nu* curve for each Q_s in figure 2(*b*).

The above analysis provides a relationship between Nu and S, thus suggesting that the heat transfer in RBC can be controlled by simply changing S. However, an obvious question remains: why does a stronger large-scale circulation shown in figure 2(*a*) lead to a reduced Nu for side-heated RBC? In the next subsection, we will measure the true heat flux by redefining the Nusselt number, and show how large-scale circulation enhances the heat transfer of side-heated RBC.

3.3. *Redefined Nusselt number and its enhancement*

In this subsection, we redefine the Nusselt number by counting all heat inputs to the RBC system as the total convective heat Q^*_{conv}, and compare it with the overall conductive heat Q^*_{cond} associated with the wall temperature distribution. The resulting analysis will show that the newly defined Nusselt number $Nu^* = Q^*_{conv}/Q^*_{cond}$ indeed increases with S.

As we have argued above, the sum of the side and bottom heat has to flow out through the top plate. In terms of power, the total convective power through the cell is $Q^*_{conv} = Q_t = Q_b + Q_s$, where Q_t, Q_b and Q_s represent the magnitudes of power passing through the top, bottom and side, respectively. The side heating also leads to a side temperature $T_s > T_c > T_t$, and it contributes to the total conductive heat flowing through the top plate.

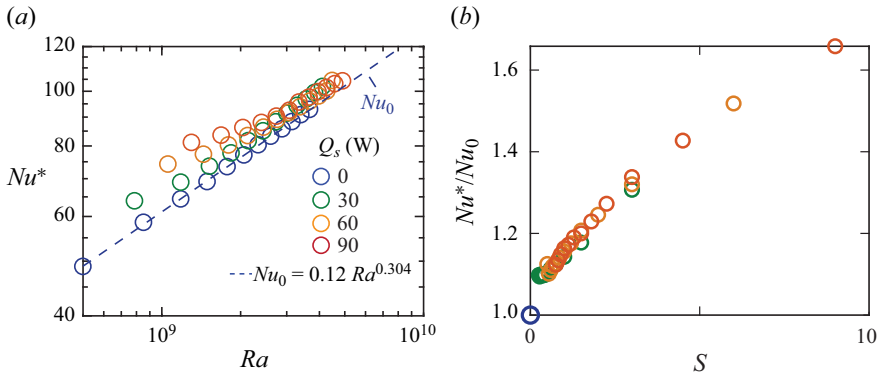

Figure 4. Redefined Nusselt number Nu^* as the ratio of total convective heat to total conductive heat. (*a*) With redefinition, data shown in figure 2(*b*) are now above the Ra–Nu_0 curve when $Q_s > 0$, showing an enhancement of heat transfer. (*b*) The ratio Nu^*/Nu_0 increases monotonically with the heating power ratio $S = Q_s/Q_b$, reaching the highest enhancement 66 % at $S = 9$ in the experiment. Plots (*a*,*b*) share the same colour scheme as in figure 2(*b*).

Hence Q^*_{cond} has to be determined by solving a steady-state heat equation with T_b, T_t and T_s satisfying Dirichlet boundary conditions for the bottom, top, and one of the sidewalls, and $\partial_n T = 0$ for the other three sidewalls. To prevent short-circuiting, the heating sidewall is separated into three regions: one central region with constant temperature T_s, and two stripes on its top and bottom with adiabatic boundary conditions, whose size matches the experimental configuration 5 : 190 : 5 mm. The steady-state heat equation $\partial_x^2 T + \partial_y^2 T = 0$, together with these mixed boundary conditions, can be solved numerically. Here, we use a finite elements package COMSOL Multiphysics with MATLAB Livelink, and compute the conductive heat in two dimensions, as we assume no significant structural change in the third direction. The overall conductive heat transfer rate, computed along the top boundary, is thus determined as $Q^*_{cond} = -\lambda L \int_0^L (\partial T/\partial y)(x, L)\,\mathrm{d}x$.

As shown in figure 4(*a*), the redefined $Nu^* = Q^*_{conv}/Q^*_{cond}$ for each Ra and $S > 0$ lies above the unperturbed Ra–Nu_0 curve (dashed line in figure 4*a*), indicating that side heating indeed results in a higher heat transfer rate. At large Ra (small S), the contribution from the bottom heating Q_b dominates the overall heat transfer, so the classical Nu_0–Ra relationship becomes the asymptotic limit. At small Ra (large S), however, the redefined Nu^* deviates from the conventional power-law scaling. The degree of this enhancement, measured as Nu^*/Nu_0 in figure 4(*b*), increases monotonically with S and reaches enhancement 66 % at $S = 9$ – the highest S reached in our experiments. We attribute this Nu^* boost to the strengthening of large-scale circulation due to side heating, which enhances the bulk mixing and perhaps thins the boundary layers (figure 3*d*).

4. Discussion

Through laboratory experiments, we have investigated the effects of adding side heating to the classical RBC system. In particular, we have found an empirical law $Nu(S) = Nu_0(1 + \gamma S^{4/5})^{-1}$, which deviates from the classical Nu–Ra scaling. We further show that a redefinition of Nu is required to capture the unconventional boundary conditions in our study, and the redefined Nu^* increases monotonically with the side-heating power, thus allowing for a direct control to the RBC.

Such controllability was also demonstrated in Huang & Zhang (2022), where adjusting the horizontal heat flux leads to a response of Nu similar to figure 4(*a*). In that work, Nu also increases monotonically with S, with the highest relative enhancement achieved near the critical Rayleigh number. In the limit $S \to 0$, the horizontal flux becomes negligible compared to the vertical one, so $Nu \to Nu_0$ and the RBC converges to the classic configuration asymptotically. On the other hand, taking $S \gg 1$ would bring the system closer to the configuration of Belmonte *et al.* (1995), which is an RBC that is turned 90° to the side.

Thus both the present experiment and the previous numerical simulation (Huang & Zhang 2022) provide a simple means of controlling the RBC – adjust the horizontal heat flux, and the vertical flux responds accordingly. In electronics, current is a direct analogy to the heat flux in thermal dynamics. Therefore, our side-heated RBC functions much like an electronic NPN transistor, where the current flowing between the collector and the emitter can be controlled by adding a current to the base (Scherz & Monk 2013).

But unlike the electronic transistors, the response of our 'thermal transistor' is slow, usually taking hours to reach dynamical equilibrium after adjusting the side-heating power. In Huang & Zhang (2022), we have experimented with a time-dependent perturbation and identified a relaxation time for the system to reach dynamical equilibrium. How does the side-heated RBC respond to a change of side-heating power? Our observation is that bulk quantities such as Re and Nu relax to their equilibrium values exponentially, with a relaxation time scale of hours.

With water as the working fluid, the Ra range for the present study is limited. We plan to conduct numerical studies and also work with other fluids to extend this range of Ra. At very high Ra, the RBC will transition into its ultimate regime (Lohse & Shishkina 2023), and a noticeable perturbation from the side heating would require a significantly higher power in that case. However, at very low Ra, the fluid may stay in place if Ra is below its critical value – side heating could thereby bring motion to an otherwise motionless fluid. A more detailed perturbation study is currently underway, and we hope to better understand the dynamical interplay between the boundary conditions and the bulk fluid through such fluid–structure interaction investigations.

Acknowledgements. We thank S. Childress, M. Shelley, J.-Q. Zhong and L. Ristroph for helpful discussions.

Funding. We acknowledge funding provided by the National Natural Science Foundation of China (92252204, 12272237) and the NYU Shanghai Major Grants Seed Fund.

Declaration of interests. The authors report no conflict of interest.

Author ORCID.
Jinzi Mac Huang https://orcid.org/0000-0003-4277-5851.

References

Ahlers, G., Grossmann, S. & Lohse, D. 2009 Heat transfer and large scale dynamics in turbulent Rayleigh–Bénard convection. *Rev. Mod. Phys.* **81** (2), 503.

Bao, Y., Chen, J., Liu, B.-F., She, Z.-S., Zhang, J. & Zhou, Q. 2015 Enhanced heat transport in partitioned thermal convection. *J. Fluid Mech.* **784**, R5.

Barry, R.G. 1992 *Mountain Weather and Climate*. Psychology Press.

Belmonte, A., Tilgner, A. & Libchaber, A. 1994 Temperature and velocity boundary layers in turbulent convection. *Phys. Rev.* E **50** (1), 269.

Belmonte, A., Tilgner, A. & Libchaber, A. 1995 Turbulence and internal waves in side-heated convection. *Phys. Rev.* E **51**, 5681–5687.

Chong, K.L. & Xia, K.-Q. 2016 Exploring the severely confined regime in Rayleigh–Bénard convection. *J. Fluid Mech.* **805**, R4.

DU, Y.-B. & TONG, P. 1998 Enhanced heat transport in turbulent convection over a rough surface. *Phys. Rev. Lett.* **81**, 987–990.

DUDOK DE WIT, T., *et al.* 2020 Switchbacks in the near-Sun magnetic field: long memory and impact on the turbulence cascade. *Astrophys. J. Suppl. Ser.* **246** (2), 39.

EMANUEL, K.A. 1994 *Atmospheric Convection*. Oxford University Press.

FUNFSCHILLING, D., BROWN, E., NIKOLAENKO, A. & AHLERS, G. 2005 Heat transport by turbulent Rayleigh–Bénard convection in cylindrical samples with aspect ratio one and larger. *J. Fluid Mech.* **536**, 145–154.

GROSSMANN, S. & LOHSE, D. 2000 Scaling in thermal convection: a unifying theory. *J. Fluid Mech.* **407**, 27–56.

HUANG, J.M. 2024 Covering convection with a thermal blanket: numerical simulation and stochastic modelling. *J. Fluid Mech.* **980**, A47.

HUANG, J.M. & ZHANG, J. 2022 Rayleigh–Bénard thermal convection perturbed by a horizontal heat flux. *J. Fluid Mech.* **954**, R2.

HUANG, J.M., ZHONG, J.-Q., ZHANG, J. & MERTZ, L. 2018 Stochastic dynamics of fluid–structure interaction in turbulent thermal convection. *J. Fluid Mech.* **854**, R5.

HUANG, S.-D. & XIA, K.-Q. 2016 Effects of geometric confinement in quasi-2-D turbulent Rayleigh–Bénard convection. *J. Fluid Mech.* **794**, 639–654.

HUGHES, G.O. & GRIFFITHS, R.W. 2008 Horizontal convection. *Annu. Rev. Fluid Mech.* **40**, 185–208.

JIANG, H., ZHU, X., MATHAI, V., VERZICCO, R., LOHSE, D. & SUN, C. 2018 Controlling heat transport and flow structures in thermal turbulence using ratchet surfaces. *Phys. Rev. Lett.* **120**, 044501.

JORGENSEN, D.P. & LEMONE, M.A. 1989 Vertical velocity characteristics of oceanic convection. *J. Atmos. Sci.* **46** (5), 621–640.

LOHSE, D. & SHISHKINA, O. 2023 Ultimate turbulent thermal convection. *Phys. Today* **76** (11), 26–32.

LOHSE, D. & XIA, K.-Q. 2010 Small-scale properties of turbulent Rayleigh–Bénard convection. *Annu. Rev. Fluid Mech.* **42** (1), 335–364.

MEAKIN, P. & JAMTVEIT, B. 2010 Geological pattern formation by growth and dissolution in aqueous systems. *Proc. R. Soc.* A **466** (2115), 659–694.

MILLER, R.C. 1968 A thermally convecting fluid heated non-uniformly from below. PhD thesis, Massachusetts Institute of Technology.

NIEMELA, J.J., SKRBEK, L., SREENIVASAN, K.R. & DONNELLY, R.J. 2000 Turbulent convection at very high Rayleigh numbers. *Nature* **404** (6780), 837–840.

NORDLUND, Å. 1985 Solar convection. *Sol. Phys.* **100** (1–2), 209–235.

SALMON, R. 1998 *Lectures on Geophysical Fluid Dynamics*. Oxford University Press.

SCHERZ, P. & MONK, S. 2013 *Practical Electronics for Inventors*, 3rd edn. McGraw-Hill Education.

SCHLICHTING, H. & GERSTEN, K. 2003 *Boundary Layer Theory*. Springer.

STEIN, R.F. & NORDLUND, A. 1989 Topology of convection beneath the solar surface. *Astrophys. J.* **342**, L95–L98.

STEVENS, R.J.A.M., LOHSE, D. & VERZICCO, R. 2014 Sidewall effects in Rayleigh–Bénard convection. *J. Fluid Mech.* **741**, 1–27.

STEVENS, R.J.A.M., VAN DER POEL, E.P., GROSSMANN, S. & LOHSE, D. 2013 The unifying theory of scaling in thermal convection: the updated prefactors. *J. Fluid Mech.* **730**, 295–308.

STEVENS, R.J.A.M., ZHONG, J.-Q., CLERCX, H.J.H., AHLERS, G. & LOHSE, D. 2009 Transitions between turbulent states in rotating Rayleigh–Bénard convection. *Phys. Rev. Lett.* **103**, 024503.

TILGNER, A., BELMONTE, A. & LIBCHABER, A. 1993 Temperature and velocity profiles of turbulent convection in water. *Phys. Rev.* E **47** (4), R2253.

VALLIS, G.K. 2006 *Atmospheric and Oceanic Fluid Dynamics: Fundamentals and Large-scale Circulation*. Cambridge University Press.

WANG, K. & ZHANG, J. 2023 Persistent corotation of the large-scale flow of thermal convection and an immersed free body. *Proc. Natl Acad. Sci.* **120** (21), e2217705120.

WANG, W. & HUANG, R.X. 2005 An experimental study on thermal circulation driven by horizontal differential heating. *J. Fluid Mech.* **540**, 49–73.

XIA, K.-Q. & LUI, S.-L. 1997 Turbulent thermal convection with an obstructed sidewall. *Phys. Rev. Lett.* **79** (25), 5006.

ZHANG, J., CHILDRESS, S. & LIBCHABER, A. 1997 Non-Boussinesq effect: thermal convection with broken symmetry. *Phys. Fluids* **9** (4), 1034–1042.

ZHONG, J.-Q. & AHLERS, G. 2010 Heat transport and the large-scale circulation in rotating turbulent Rayleigh–Bénard convection. *J. Fluid Mech.* **665**, 300–333.

ZHONG, J.-Q., STEVENS, R.J.A.M., CLERCX, H.J.H., VERZICCO, R., LOHSE, D. & AHLERS, G. 2009 Prandtl-, Rayleigh-, and Rossby-number dependence of heat transport in turbulent rotating Rayleigh–Bénard convection. *Phys. Rev. Lett.* **102**, 044502.

ZHONG, J.-Q. & ZHANG, J. 2005 Thermal convection with a freely moving top boundary. *Phys. Fluids* **17** (11), 115105.